

**Chirality-dependent frequency shift of radial breathing mode in metallic carbon nanotubes**Ken-ichi Sasaki,<sup>1</sup> Riichiro Saito,<sup>1</sup> Gene Dresselhaus,<sup>2</sup> Mildred S. Dresselhaus,<sup>3,4</sup> Hootan Farhat,<sup>5</sup> and Jing Kong<sup>4</sup><sup>1</sup>*Department of Physics, Tohoku University and CREST-JST, Sendai, 980-8578, Japan*<sup>2</sup>*Francis Bitter Magnet Laboratory, Cambridge, Massachusetts 02139-4307, USA*<sup>3</sup>*Department of Physics, Massachusetts Institute of Technology, Cambridge, Massachusetts 02139-4307, USA*<sup>4</sup>*Department of Electrical Engineering and Computer Science, Massachusetts Institute of Technology, Cambridge, Massachusetts 02139-4307, USA*<sup>5</sup>*Department of Materials Science and Engineering, Massachusetts Institute of Technology, Cambridge, Massachusetts 02139-4307, USA*

(Received 16 September 2008; revised manuscript received 3 November 2008; published 2 December 2008)

A phonon frequency shift of the radial breathing mode for metallic single wall carbon nanotubes is predicted as a function of Fermi energy. Armchair nanotubes do not show any frequency shift while zigzag nanotubes exhibit phonon softening, but this softening is not associated with the broadening. This chirality dependence originates from a curvature-induced energy gap and a special electron-phonon coupling mechanism for radial breathing modes. Because of the particle-hole symmetry, only the off-site deformation potential contributes to the frequency shift. On the other hand, the on-site potential contributes to the Raman intensity, and the radial breathing mode intensity is stronger than that of the  $G$  band. The relationship between the chirality dependence of the frequency shift of the radial breathing mode and the  $\Gamma$  point optical-phonon frequency shift is discussed.

DOI: [10.1103/PhysRevB.78.235405](https://doi.org/10.1103/PhysRevB.78.235405)

PACS number(s): 61.46.-w, 63.22.-m

**I. INTRODUCTION**

Raman spectroscopy has been widely used for the characterization of carbon nanotube<sup>1-6</sup> and graphene<sup>7-9</sup> samples, since Raman spectroscopy is a nondestructive and noncontact measurement that can be carried out under ambient air pressure and at room temperature. The  $G$  band which gives a strong Raman intensity at around  $1600\text{ cm}^{-1}$  ( $\approx 0.2\text{ eV}$ ) in graphene consists of the  $\Gamma$  point longitudinal-optical (LO) and transverse-optical (TO)-phonon modes.<sup>10</sup> For single wall carbon nanotubes (SWNTs), these two phonon modes with  $A_{1g}$  symmetry split by the curvature effect into two Raman features which we call the  $G^+$  and  $G^-$  bands.<sup>11</sup> It has been observed for metallic SWNTs that the peak positions of the  $G^+$  and  $G^-$  features shift differently from each other as a function of the Fermi energy  $E_F$ .<sup>12-15</sup> It is known that virtual electron-hole pair creation by the electron-phonon (el-ph) interaction gives a self-energy correction to the phonon frequency, which is relevant to the phonon frequency shift. The behavior of the  $G^+$  and  $G^-$  bands indicates that the el-ph interactions for the  $\Gamma$  point LO/TO modes appear to be different from each other in metallic SWNTs. The frequency shift for the LO/TO mode for graphene and nanotubes has been discussed by many authors.<sup>16-25</sup> In a previous paper, we showed that the phonon softening for the LO and TO phonon is chirality dependent in which the curvature effect is important.<sup>26</sup> For example, only armchair SWNTs do not exhibit any frequency shift of the TO mode due to the absence of a curvature-induced energy gap in armchair SWNTs.

A similar effect may be observed for the radial breathing mode (RBM) which appears in the SWNT Raman spectra at around  $240\text{ cm}^{-1}$  ( $\approx 30\text{ meV}$ ) for a nanotube diameter of around  $d_t \approx 1\text{ nm}$ . The RBM is often used to assign the diameter and chirality of a nanotube.<sup>4,27,28</sup> For metallic SWNTs except for armchair SWNTs, the curvature of a cylindrical graphene layer induces a small energy gap.<sup>29-31</sup> Since the curvature-induced energy gap has a similar energy to that for

the RBM, especially for SWNTs with diameter less than 2 nm, the curvature-induced energy gap may affect the phonon softening of the RBM, which is the motivation of the present paper. Thus, it is important to estimate this frequency shift of the RBM for metallic SWNTs. In this paper, we examine the dependence of the RBM frequency shift on  $E_F$  and chirality for metallic SWNTs. The relationship between the RBM and the LO/TO modes is examined for the el-ph matrix element of the electron-hole pair creation.

Since the frequency shift of a phonon mode is mainly due to a low-energy electron-hole pair creation, a theory for electrons near the Fermi energy is useful for calculating the matrix element for an electron-hole pair creation. The el-ph interaction has previously been examined in terms of an effective-mass model by several authors.<sup>19,32</sup> It is known that the el-ph interaction consists of on-site and off-site terms. The on-site term represents a process whereby a  $\pi$  electron changes its energy due to a deformation potential but stays at the same position. The off-site term on the other hand represents a scattering process whereby a  $\pi$  electron moves into a nearest carbon site due to a deformation potential.<sup>33</sup> As for the  $\Gamma$  point LO/TO modes, the el-ph interaction is given only by the off-site term. In a previous paper, we showed that the off-site term of the el-ph interaction becomes sensitive to the position of the cutting line or to the curvature effect.<sup>26</sup> In this paper, we will show that an interesting property of the RBM is that the el-ph interaction is given not only by the off-site term but also by the on-site term. Although the on-site term does not contribute to the frequency shift of the RBM because of the particle-hole symmetry about the Dirac point, the on-site term of the el-ph interaction enhances the Raman intensity of the RBM.

This paper is organized as follows. In Sec. II we show that the curvature-induced energy gap determines the basic features for the frequency shift of the RBM. In Sec. III, we show the el-ph interaction for the RBM using an effective-mass model for a graphene sheet with a lattice deformation.

In Sec. IV, we calculate the frequency shift of the RBM as a function of the Fermi energy. We compare our results with experimental data in Sec. V. A discussion and summary of these effects are given in Sec. VI. The effective-mass Hamiltonian used in Secs. III and IV is derived in Appendixes A and B, respectively.

## II. RADIAL BREATHING MODE AND THE CURVATURE-INDUCED ENERGY GAP

Here we show that the basic features of the frequency shift of the RBM are determined by the curvature-induced energy gap. A renormalized RBM energy becomes  $\hbar\omega = \hbar\omega^{(0)} + \hbar\omega^{(2)}$  where  $\omega^{(0)}$  is the unperturbed RBM frequency and  $\omega^{(2)}$  is the quantum correction to the RBM frequency due to the el-ph interaction. We assume that  $\omega^{(0)}$  is a monotonic function of the tube diameter [ $d_t$  (nm)] and is modeled as linear in inverse diameter with an offset as

$$\omega^{(0)} = \frac{c_1}{d_t} + c_2, \quad (1)$$

where  $c_1 = 223.5$  ( $\text{cm}^{-1}$ ) and  $c_2 = 12.5$  ( $\text{cm}^{-1}$ ) are experimentally derived parameters as obtained by Bachilo *et al.*,<sup>34,35</sup> while  $\hbar\omega^{(2)}$  is calculated by second-order perturbation theory<sup>26</sup> as

$$\hbar\omega^{(2)} = 2 \sum_{\mathbf{k}} \frac{|\langle e\mathbf{h}(\mathbf{k}) | \mathcal{H}_{ep} | \omega^{(0)} \rangle|^2}{\hbar\omega^{(0)} - [E_e(\mathbf{k}) - E_h(\mathbf{k})] + i\Gamma} \times \{f[E_h(\mathbf{k}) - E_F] - f[E_e(\mathbf{k}) - E_F]\}. \quad (2)$$

In Eq. (2), the factor of 2 comes from spin degeneracy,  $E_e(\mathbf{k})$  [ $E_h(\mathbf{k})$ ] is the energy of an electron (hole) with wave vector  $\mathbf{k}$ ,  $\langle e\mathbf{h}(\mathbf{k}) | \mathcal{H}_{ep} | \omega^{(0)} \rangle$  is the el-ph matrix element that the RBM changes into an electron-hole pair with wave vector  $\mathbf{k}$  [see Fig. 1(a)], and  $f[x]$  is the Fermi function. We obtain  $\Gamma$  (the half of the decay width) by calculating  $\Gamma = -\text{Im}(\hbar\omega^{(2)})$  self-consistently in Eq. (2).

We consider the real and imaginary parts of the denominator of Eq. (2),  $h(E) = 1/(\hbar\omega^{(0)} - E + i\Gamma)$ , as a function of the energy of an intermediate electron-hole pair state  $E \equiv E_e(\mathbf{k}) - E_h(\mathbf{k})$  [see Fig. 1(b)].  $\text{Re}[h(E)]$  has a positive (negative) value when  $E < \hbar\omega^{(0)}$  ( $E > \hbar\omega^{(0)}$ ), and the lower (higher) energy electron-hole pair makes a positive (negative) contribution to  $\hbar\omega^{(2)}$ . Therefore, the sign of the contribution to  $\text{Re}(\hbar\omega^{(2)})$ , i.e., frequency hardening or softening, depends on its electron-hole virtual state energy  $E$ . The curvature-induced energy gap  $E_{\text{gap}}$  affects the RBM frequency shift since an electron-hole pair creation is possible only when  $E \geq E_{\text{gap}}$ . When  $0 < E_{\text{gap}} \leq \hbar\omega^{(0)}$ , the contribution to frequency hardening in Eq. (2) is suppressed. When  $E_{\text{gap}} > \hbar\omega^{(0)}$ , not only are all the positive contributions to the RBM frequency suppressed, but some negative contributions are also suppressed. Further,  $\text{Im}[h(E)]$  is nonzero only when  $E$  is very close to  $\hbar\omega^{(0)}$ , which shows that the RBM phonon can resonantly decay into an electron-hole pair with the same energy. This means that  $\Gamma \approx 0$  when  $E_{\text{gap}} > \hbar\omega^{(0)}$  because no electron-hole pair excitation is allowed near  $E = \hbar\omega^{(0)}$ . Thus, it is important to compare the values of  $E_{\text{gap}}$  and  $\hbar\omega^{(0)}$  for each  $(n, m)$  SWNT.

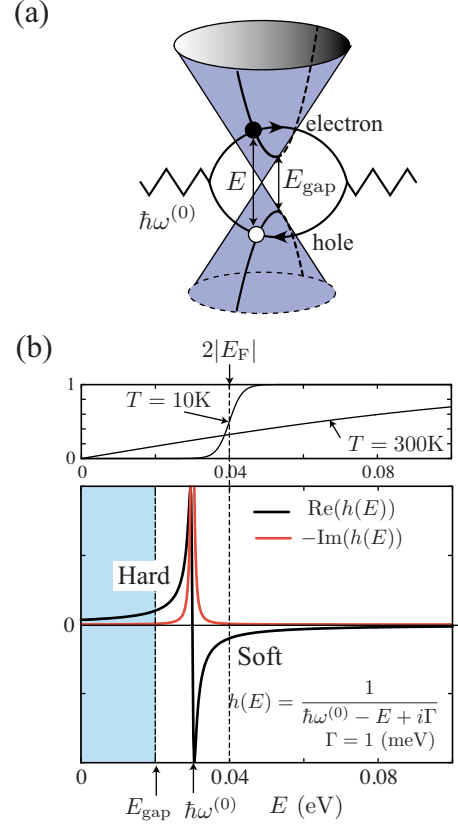


FIG. 1. (Color online) (a) An intermediate electron-hole pair consists of an electron in the conduction band and a hole in the valence band. The RBM is denoted by a zigzag line and an electron-hole pair is represented by a loop. A cutting line for a metallic SWNT is shown as the solid curve projected on the surface of the Dirac cone. The electron-hole pair creation is possible only when  $E \geq E_{\text{gap}}$ . (b) The energy correction to the phonon energy by an intermediate electron-hole pair, especially the sign of  $\text{Re}[h(E)]$  (black curve), that is, frequency hardening or softening, depends on the energy of the intermediate state  $E$ . The contribution to  $\hbar\omega^{(2)}$  of a low-energy electron-hole pair satisfying  $0 \leq E \leq E_{\text{gap}}$  is forbidden.  $\text{Im}[h(E)]$  (red curve) is nonzero only when  $E$  is very close to  $\hbar\omega^{(0)}$ , which shows that the RBM can resonantly decay into an electron-hole pair with the same energy. The figure is the case of  $\hbar\omega^{(0)} = 30$  meV,  $E_{\text{gap}} = 20$  meV. The Fermi distribution function  $f[E_h(\mathbf{k}) - E_F] - f[E_e(\mathbf{k}) - E_F]$  is plotted for  $T = 10$  K and  $T = 300$  K as a function of  $E$  in the case of  $|E_F| = 20$  meV.

In Fig. 2(a) we plot  $E_{\text{gap}}$  for each  $(n, m)$  for metallic SWNTs as a function of the chiral angle  $\theta$  ( $^\circ$ ) and tube diameter  $d_t$  (nm). We performed the energy-band-structure calculation in an extended tight-binding framework<sup>36</sup> to obtain  $E_{\text{gap}}$ . Figure 2(a) shows that for a fixed  $d_t$ , a zigzag SWNT ( $\theta = 0^\circ$ ) has the largest value of  $E_{\text{gap}}$  and an armchair SWNT ( $\theta = 30^\circ$ ) has no energy gap. The  $(n, m)$  values associated with a curve are given by  $n - m = 3q$  ( $q = 0, 1, 2, \dots$ ). The calculated results are well reproduced by

$$E_{\text{gap}} = \frac{c}{d_t^2} \cos 3\theta, \quad (3)$$

with  $c = 60$  ( $\text{meV nm}^2$ ).<sup>37</sup> Using Eqs. (1) and (3) for zigzag SWNTs ( $\theta = 0^\circ$ ), we see that  $E_{\text{gap}}$  is larger than  $\hbar\omega^{(0)}$  when

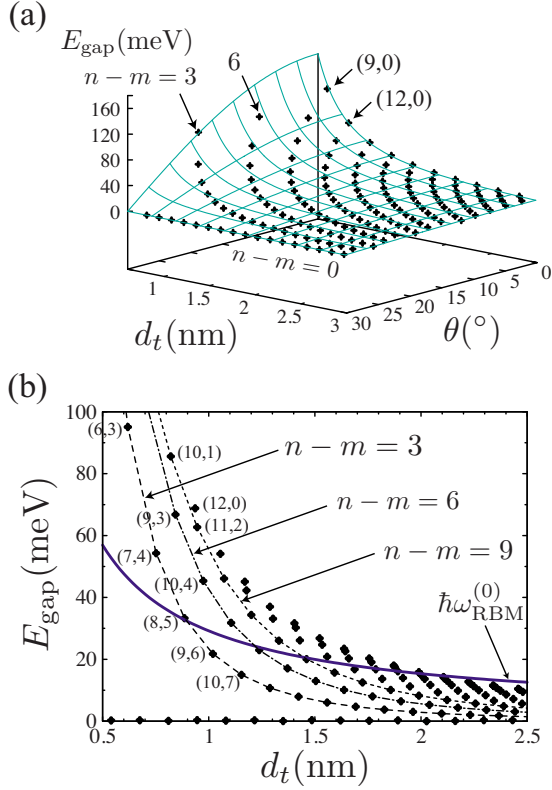


FIG. 2. (Color online) (a) The dependence of the curvature-induced energy gap  $E_{\text{gap}}$  on the chiral angle  $\theta$  and tube diameter  $d_t$ . The surface is a plot of Eq. (3) which reproduces well the calculated results. (b) The  $d_t$  dependence of  $E_{\text{gap}}$ , which is given as a one-dimensional projection of (a) onto the  $d_t$  axis. We plot the energy of the RBM,  $\hbar\omega^{(0)}$  of Eq. (1), as a solid blue curve for comparison. The points on the dashed, dot-dashed, and dotted curves satisfy  $n-m=3, 6, 9$ , respectively.

$d_t \lesssim 2$  nm [see Fig. 2(b)]. Thus, no decay process (or spectral broadening) contributing to  $\Gamma$  is available for a zigzag SWNT with  $d_t \lesssim 2$  nm. On the other hand, a decay process contributing to  $\Gamma$  is available regardless of the chirality of a metallic SWNT with  $d_t \gtrsim 2$  nm. For example, in Fig. 2(b), we see that a (12,0) tube does not exhibit a finite value of  $\Gamma$  even though we get a finite value for the el-ph matrix element, but (9,6) and (10,7) may exhibit a broadening.

In addition, because of the Fermi distribution function  $f[x]$  in Eq. (2), an electron-hole pair satisfying  $E < 2|E_F|$  cannot contribute to the energy shift at zero temperature due to the Pauli principle. At zero temperature, when  $|E_F| \approx \hbar\omega^{(0)}/2$ , then  $\hbar\omega^{(2)}$  takes a minimum value since all positive contributions to  $\hbar\omega^{(2)}$  are suppressed in Eq. (2).<sup>26</sup>  $E_F$  and  $E_{\text{gap}}$  play a very similar role at zero temperature, but their difference becomes clear at a finite temperature. For example, when  $E_{\text{gap}} < \hbar\omega^{(0)}$ , then  $\Gamma$  can be nonzero even when  $2|E_F| > \hbar\omega^{(0)}$ . On the other hand, when  $E_{\text{gap}} > \hbar\omega^{(0)}$ , then  $\hbar\omega^{(2)}$  does not have an imaginary part ( $\Gamma=0$ ) even at room temperature regardless of the value of  $E_F$ . This difference between  $E_F$  and  $E_{\text{gap}}$  is understood in Eq. (2) as  $\langle \text{eh}(\mathbf{k}) | \mathcal{H}_{\text{ep}} | \omega^{(0)} \rangle = 0$  for  $E \leq E_{\text{gap}}$  and as that  $f[E_h(\mathbf{k}) - E_F] - f[E_e(\mathbf{k}) - E_F]$  is not zero for  $E < 2|E_F|$  (at a finite temperature) as shown in Fig. 1(b). Thus,  $E_{\text{gap}}$  determines whether a

SWNT can exhibit a broadening. It is pointed out that the energy band gap of a SWNT is affected by uniaxial and torsional strain as clarified by Yang *et al.*<sup>38,39</sup>

### III. ELECTRON-PHONON INTERACTION BY EFFECTIVE-MASS THEORY

Next we show the el-ph interaction in the Hamiltonian by effective-mass theory, which is used for calculating the matrix element of the el-ph interaction. We will derive Eqs. (4), (8), and (9) from the nearest-neighbor tight-binding Hamiltonian in Appendix A.<sup>40</sup>

#### A. Unperturbed Hamiltonian

The unperturbed Hamiltonian in the effective-mass model for  $\pi$  electrons near the  $K$  point of a graphene sheet is given by

$$\mathcal{H}_0^K = v_F \boldsymbol{\sigma} \cdot \hat{\mathbf{p}}, \quad (4)$$

where  $v_F$  is the Fermi velocity,  $\hat{\mathbf{p}} = -i\hbar\nabla$  is the momentum operator, and  $\boldsymbol{\sigma} = (\sigma_x, \sigma_y)$  is the Pauli matrix.  $\mathcal{H}_0^K$  is a  $2 \times 2$  matrix which operates on the two component wave function,

$$\psi^K(\mathbf{r}) = \begin{pmatrix} \psi_A^K(\mathbf{r}) \\ \psi_B^K(\mathbf{r}) \end{pmatrix}, \quad (5)$$

where  $\psi_A^K(\mathbf{r})$  and  $\psi_B^K(\mathbf{r})$  are the wave functions of  $\pi$  electrons for the sublattices A and B, respectively, around the  $K$  point. The energy eigenvalue of Eq. (4) is given by  $\pm v_F |\mathbf{p}|$  and the energy dispersion relation shows a linear dependence at the Fermi point,<sup>10</sup> which is known as the Dirac cone. The eigenstates for  $E = +v_F |\mathbf{p}|$  and  $E = -v_F |\mathbf{p}|$  are given by

$$\begin{aligned} \psi_{c,\mathbf{k}}^K(\mathbf{r}) &= \frac{e^{i\mathbf{k}\cdot\mathbf{r}}}{\sqrt{2S}} \begin{pmatrix} e^{-i\Theta(\mathbf{k})/2} \\ e^{+i\Theta(\mathbf{k})/2} \end{pmatrix}, \\ \psi_{v,\mathbf{k}}^K(\mathbf{r}) &= \frac{e^{i\mathbf{k}\cdot\mathbf{r}}}{\sqrt{2S}} \begin{pmatrix} e^{-i\Theta(\mathbf{k})/2} \\ -e^{+i\Theta(\mathbf{k})/2} \end{pmatrix}, \end{aligned} \quad (6)$$

which are a conduction state and a valence state with wave vector  $\mathbf{k}$ , respectively. In Eq. (6),  $S$  denotes the surface area of graphene, the wave vector is measured from the  $K$  point, and  $\Theta(\mathbf{k})$  is defined by an angle of  $\mathbf{k} = (k_x, k_y)$  measured from the  $k_x$  axis as  $(k_x, k_y) \equiv |\mathbf{k}| [\cos \Theta(\mathbf{k}), \sin \Theta(\mathbf{k})]$ . Here the  $k_y$  axis is defined by the direction of a zigzag nanotube axis [see the coordinate system in Fig. 3(a)]. The energy eigenstate for the valence band  $\psi_{v,\mathbf{k}}^K(\mathbf{r})$  is given by  $\sigma_z \psi_{c,\mathbf{k}}^K(\mathbf{r})$ . This results from the particle-hole symmetry of the Hamiltonian:  $\sigma_z \mathcal{H}_0^K \sigma_z = -\mathcal{H}_0^K$ . The dynamics of  $\pi$  electrons near the  $K'$  point relates to the electrons near the  $K$  point by time-reversal symmetry  $\psi^K \rightarrow (\psi^{K'})^*$ . Because lattice vibrations do not break time-reversal symmetry, we only consider the electrons near the  $K$  point in this paper.

#### B. Perturbation

Lattice deformation modifies the nearest-neighbor hopping integral locally as  $-\gamma_0 \rightarrow -\gamma_0 + \delta\gamma_0^a(\mathbf{r}_i)$  ( $a=1, 2, 3$ ) [see

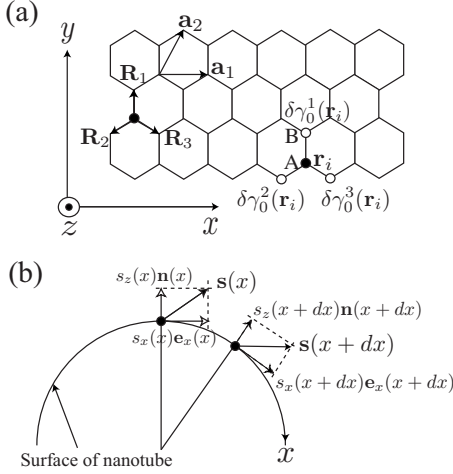


FIG. 3. (a) A hexagonal unit cell of graphene consists of  $A$  (closed circle) and  $B$  (open circle) atoms.  $\mathbf{a}_1$  and  $\mathbf{a}_2$  are lattice vectors.  $\mathbf{R}_a$  ( $a=1,2,3$ ) are vectors pointing to the nearest-neighbor  $B$  sites from an  $A$  site. For the coordinate system of  $(x,y)$ , the  $\mathbf{R}_a$  ( $a=1,2,3$ ) are written, respectively, as  $\mathbf{R}_1=a_{cc}\mathbf{e}_y$ ,  $\mathbf{R}_2=-\sqrt{3}/2a_{cc}\mathbf{e}_x-(1/2)a_{cc}\mathbf{e}_y$ , and  $\mathbf{R}_3=\sqrt{3}/2a_{cc}\mathbf{e}_x-(1/2)a_{cc}\mathbf{e}_y$  where  $a_{cc}$  is the carbon-carbon bond length and  $\mathbf{e}_x$  ( $\mathbf{e}_y$ ) is the dimensionless unit vector for the  $x$  axis ( $y$  axis). Local modulations of the hopping integral are defined by  $\delta\gamma_0^a(\mathbf{r}_i)$  ( $a=1,2,3$ ) where  $\mathbf{r}_i$  is the position of an  $A$  atom. (b) The displacement vector for the RBM,  $\mathbf{s}(x)$ , is decomposed in terms of the normal  $s_z(x)$  and tangential  $s_x(x)$  components. The derivative of the normal unit vector  $\mathbf{n}(x)$  with respect to  $x$  gives a component along  $\mathbf{e}_x(x)$ , which modifies the net displacement along the  $x$  direction.

Fig. 3(a)]. The corresponding perturbation of the lattice deformation is given by

$$\mathcal{H}_1 \equiv \sum_{i \in A} \sum_{a=1,2,3} \delta\gamma_0^a(\mathbf{r}_i) [(c_{i+a}^B)^\dagger c_i^A + (c_i^A)^\dagger c_{i+a}^B], \quad (7)$$

where  $c_i^A$  is the annihilation operator of a  $\pi$  electron of an  $A$  atom at position  $\mathbf{r}_i$ , and  $(c_{i+a}^B)^\dagger$  is a creation operator of position  $\mathbf{r}_{i+a}$  ( $=\mathbf{r}_i+\mathbf{R}_a$ ) of a  $B$  atom where  $\mathbf{R}_a$  ( $a=1,2,3$ ) are vectors pointing to the three nearest-neighbor  $B$  sites from an  $A$  site [see Fig. 3(a)].

The perturbation of Eq. (7) gives rise to scattering within a region near the  $K$  point (intravalley scattering) whose interaction is given by a deformation-induced gauge field  $\mathbf{A}(\mathbf{r})=[A_x(\mathbf{r}), A_y(\mathbf{r})]$  in Eq. (4) as

$$v_F \boldsymbol{\sigma} \cdot [\hat{\mathbf{p}} + \mathbf{A}(\mathbf{r})]. \quad (8)$$

$\mathbf{A}(\mathbf{r})$  is defined from  $\delta\gamma_0^a(\mathbf{r})$  ( $a=1,2,3$ ) as<sup>40,41</sup>

$$v_F A_x(\mathbf{r}) = \delta\gamma_0^1(\mathbf{r}) - \frac{1}{2}[\delta\gamma_0^2(\mathbf{r}) + \delta\gamma_0^3(\mathbf{r})],$$

$$v_F A_y(\mathbf{r}) = \frac{\sqrt{3}}{2}[\delta\gamma_0^2(\mathbf{r}) - \delta\gamma_0^3(\mathbf{r})]. \quad (9)$$

When  $\delta\gamma_0^2=\delta\gamma_0^3=0$ , then  $\mathbf{A}(\mathbf{r})=[A_x(\mathbf{r}), 0]$  and  $\mathbf{A}(\mathbf{r}) \cdot \mathbf{R}_1=0$ . Similarly, when  $\delta\gamma_0^1=\delta\gamma_0^3=0$ , we have  $\mathbf{A}(\mathbf{r}) \cdot \mathbf{R}_2=0$ . Generally, the direction of  $\mathbf{A}(\mathbf{r})$  is pointing perpendicular to the bond whose hopping integral is changed from  $\gamma_0$ .

When the displacement vector of a carbon atom at  $\mathbf{r}$  is  $\mathbf{s}(\mathbf{r})=[s_x(\mathbf{r}), s_y(\mathbf{r}), s_z(\mathbf{r})]$ , the perturbation to the nearest-neighbor hopping integral is given by

$$\delta\gamma_0^a(\mathbf{r}) = \frac{g_{\text{off}}}{\ell a_{cc}} \mathbf{R}_a \cdot \{\mathbf{s}(\mathbf{r} + \mathbf{R}_a) - \mathbf{s}(\mathbf{r})\}, \quad (10)$$

where  $g_{\text{off}}$  is the off-site coupling constant and  $\ell=3a_{cc}/2$ . By expanding  $\mathbf{s}(\mathbf{r} + \mathbf{R}_a)$  in a Taylor series around  $\mathbf{s}(\mathbf{r})$  as  $\mathbf{s}(\mathbf{r} + \mathbf{R}_a) = \mathbf{s}(\mathbf{r}) + (\mathbf{R}_a \cdot \nabla)\mathbf{s}(\mathbf{r}) + \dots$ , we approximate Eq. (10) as

$$\delta\gamma_0^a(\mathbf{r}) \approx \frac{g_{\text{off}}}{\ell a_{cc}} \mathbf{R}_a \cdot \{(\mathbf{R}_a \cdot \nabla)\mathbf{s}(\mathbf{r})\}. \quad (11)$$

Putting  $\mathbf{R}_1=a_{cc}\mathbf{e}_y$ ,  $\mathbf{R}_2=-\sqrt{3}/2a_{cc}\mathbf{e}_x-(1/2)a_{cc}\mathbf{e}_y$ , and  $\mathbf{R}_3=(\sqrt{3}/2)a_{cc}\mathbf{e}_x-(1/2)a_{cc}\mathbf{e}_y$ , into the right-hand side of Eq. (11), we obtain the corresponding deformation-induced gauge field of Eq. (9) as

$$v_F A_x(\mathbf{r}) = \frac{g_{\text{off}}}{2} \left[ -\frac{\partial s_x(\mathbf{r})}{\partial x} + \frac{\partial s_y(\mathbf{r})}{\partial y} \right],$$

$$v_F A_y(\mathbf{r}) = \frac{g_{\text{off}}}{2} \left[ \frac{\partial s_x(\mathbf{r})}{\partial y} + \frac{\partial s_y(\mathbf{r})}{\partial x} \right]. \quad (12)$$

Further the displacements of carbon atoms give an on-site deformation potential

$$\mathcal{H}_{\text{on}} = g_{\text{on}} \sigma_0 \left[ \frac{\partial s_x(\mathbf{r})}{\partial x} + \frac{\partial s_y(\mathbf{r})}{\partial y} \right]. \quad (13)$$

Here  $\sigma_0$  is the  $2 \times 2$  unit matrix and  $\partial s_x(\mathbf{r})/\partial x + \partial s_y(\mathbf{r})/\partial y$  represents the change in the area of a graphene sheet.<sup>32</sup> In Eqs. (12) and (13), according to the density-functional calculation by Porezag *et al.*,<sup>42</sup> we adopt the off-site coupling constant  $g_{\text{off}}=6.4$  eV and the on-site coupling constant  $g_{\text{on}}=17.0$  eV.<sup>33,43</sup>

Since Eqs. (12) and (13) are proportional to the derivatives of  $s_x(\mathbf{r})$  and  $s_y(\mathbf{r})$ , that is, they are proportional to  $\mathbf{q}$ , the el-ph matrix element for the in-plane longitudinal/transverse-acoustic (LA/TA) phonon modes vanishes at the  $\Gamma$  point where  $\mathbf{q}$  is the phonon wave vector. Namely,  $\mathbf{A}(\mathbf{r})=0$  and  $\mathcal{H}_{\text{on}}=0$  in the limit of  $\mathbf{q}=0$ . Among the TA phonon modes, there is an out-of-plane TA (oTA) phonon mode. The oTA mode shifts carbon atoms on the flat two-dimensional (2D) graphene sheet into the  $z$  direction [see Figs. 3(a) and 3(b)]. The oTA mode of graphene corresponds to the RBM of a nanotube even though the RBM is not an acoustic-phonon mode.<sup>10</sup> In the following, we will show that the el-ph interaction for the RBM is enhanced due to the curvature of the nanotube as compared with the oTA mode of graphene since the RBM is a bond-stretching mode because of the cylindrical structure of SWNTs.

The displacements of the RBM modify the radius of a nanotube as  $r \rightarrow r + s_z(\mathbf{r})$  [see Fig. 3(b)]. A change in the radius gives rise to two effects on the electronic state. One effect is a shift of the wave vector around the tube axis. The distance between two wave vectors around the tube axis depends on the inverse of the radius due to the periodic boundary condition and a change in the radius results in a shift of the wave vector. The other effect is that the RBM can change

the area on the surface of the nanotube even at the  $\Gamma$  point. This results in an enhancement of the on-site interaction. These two effects are relevant to the fact that the normal vector on the surface of a nanotube is pointing in a different direction depending on the position. To show this, we take a (zigzag) nanotube as shown in Fig. 3(b). Let us denote the displacement vectors of two carbon atoms at  $x$  and  $x+dx$  as  $\mathbf{s}(x)$  and  $\mathbf{s}(x+dx)$ , then an effective length for the displacement along the  $x$  axis between the nearest two atoms is given by

$$D_x = \mathbf{e}_x(x+dx) \cdot [\mathbf{s}(x+dx) - \mathbf{s}(x)]. \quad (14)$$

By decomposing  $\mathbf{s}(x)$  in terms of a normal and a tangential unit vector as  $\mathbf{s}(x) = s_z(x)\mathbf{n}(x) + s_x(x)\mathbf{e}_x(x)$  [see Fig. 3(b)], we see that Eq. (14) becomes

$$\begin{aligned} D_x &= s_x(x+dx) + s_z(x+dx)\mathbf{e}_x(x+dx) \cdot \mathbf{n}(x+dx) \\ &\quad - s_x(x)\mathbf{e}_x(x+dx) \cdot \mathbf{e}_x(x) - s_z(x)\mathbf{e}_x(x+dx) \cdot \mathbf{n}(x) \\ &= dx \left\{ \frac{\partial s_x(x)}{\partial x} + \frac{s_z(x)}{r} \right\} + \dots, \end{aligned} \quad (15)$$

where we have used the following equations:

$$\mathbf{n}(x+dx) = \mathbf{n}(x) + \frac{dx}{r}\mathbf{e}_x(x) + \dots,$$

$$\mathbf{e}_x(x+dx) = \mathbf{e}_x(x) + \frac{dx}{r}\mathbf{n}(x) + \dots. \quad (16)$$

Equation (15) shows that the net displacement along the  $x$  axis is modified by the curvature of the nanotube as  $\partial_x s_x(\mathbf{r}) \rightarrow \partial_x s_x(\mathbf{r}) + s_z(\mathbf{r})/r$ . The correction is negligible for a graphene sheet ( $r \rightarrow \infty$ ).

The el-ph interaction for the RBM is included by replacing  $\partial_x s_x(\mathbf{r})$  with  $\partial_x s_x(\mathbf{r}) + s_z(\mathbf{r})/r$  in Eqs. (12) and (13). In Eq. (12), we have an additional deformation-induced gauge field  $v_F A_x(\mathbf{r}) = -(g_{\text{off}}/2)(s_z(\mathbf{r})/r)$  for the RBM mode which gives rise to a shift of the wave vector around the tube axis. In Eq. (13), it is shown that the RBM produces on-site deformation potential of  $g_{\text{on}}\sigma_0[s_z(\mathbf{r})/r]$ . Finally, we obtain the el-ph interaction for the  $\Gamma$  point [ $\mathbf{q}=0$ :  $\mathbf{s}(\mathbf{r})$  is a constant] RBM, as

$$\mathcal{H}_{\text{ep}} = -\frac{g_{\text{off}}s_z}{2r}\sigma_x + g_{\text{on}}\frac{s_z}{r}\sigma_0 = \frac{2s_z}{d_t} \begin{pmatrix} g_{\text{on}} & -\frac{g_{\text{off}}}{2} \\ -\frac{g_{\text{off}}}{2} & g_{\text{on}} \end{pmatrix}. \quad (17)$$

#### IV. ELECTRON-PHONON MATRIX ELEMENT AND FREQUENCY SHIFT

In this section we calculate the el-ph matrix element for an electron-hole pair creation and the corresponding frequency shift of the RBM.

From Eqs. (6) and (17), the el-ph matrix element for an electron-hole pair generation near the  $K$  point is given by

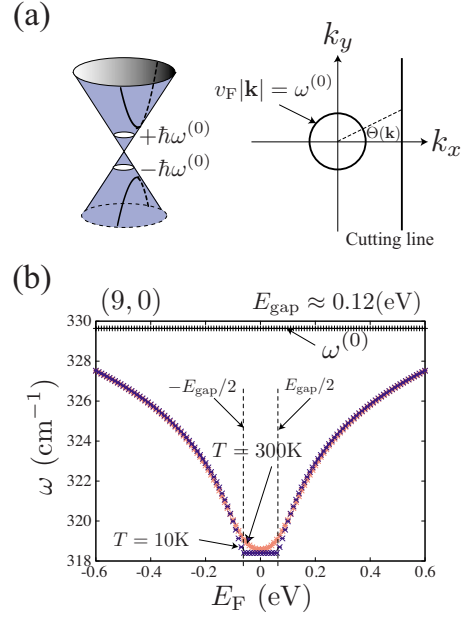


FIG. 4. (Color online) (a) The decay width is zero because of  $E_{\text{gap}} > \hbar\omega^{(0)}$ . This is shown by the relative positions of the cutting line and the equienergy contour circle satisfying  $v_F|\mathbf{k}| = \omega^{(0)}$  with respect to the Dirac point. (b) The  $E_F$  dependence of the RBM frequency in the case of the (9,0) zigzag SWNT at room temperature (red curve) and at 10 K (blue curve). We plot  $\omega^{(0)}$  as the black line for comparison.

$$\begin{aligned} &\langle e\mathbf{h}(\mathbf{k}) | \mathcal{H}_{\text{ep}} | \omega^{(0)} \rangle \\ &= \int (\psi_{c,\mathbf{k}}^K(\mathbf{r}))^\dagger \mathcal{H}_{\text{ep}} \psi_{v,\mathbf{k}}^K(\mathbf{r}) d^2\mathbf{r} \\ &= \frac{s_z}{d_t} \begin{pmatrix} e^{+i[\Theta(\mathbf{k})/2]} \\ e^{-i[\Theta(\mathbf{k})/2]} \end{pmatrix}^t \begin{pmatrix} g_{\text{on}} & -\frac{g_{\text{off}}}{2} \\ -\frac{g_{\text{off}}}{2} & g_{\text{on}} \end{pmatrix} \begin{pmatrix} e^{-i[\Theta(\mathbf{k})/2]} \\ -e^{+i[\Theta(\mathbf{k})/2]} \end{pmatrix} \\ &= ig_{\text{off}} \frac{s_z}{d_t} \sin \Theta(\mathbf{k}). \end{aligned} \quad (18)$$

It is noted that the  $g_{\text{on}}$  term does not contribute to the RBM frequency shift. This is because the particle-hole symmetry  $\psi_{v,\mathbf{k}}(\mathbf{r}) = \sigma_z \psi_{c,\mathbf{k}}(\mathbf{r})$  gives a vanishing matrix element  $\psi_{c,\mathbf{k}}^\dagger(\mathbf{r}) g_{\text{on}} \sigma_0 \psi_{v,\mathbf{k}}(\mathbf{r}) = g_{\text{on}} \psi_{c,\mathbf{k}}^\dagger(\mathbf{r}) \sigma_0 \sigma_z \psi_{c,\mathbf{k}}(\mathbf{r}) = 0$  in Eq. (18). We note that  $\sin \Theta(\mathbf{k})$  of Eq. (18) indicates that low-energy electron-hole pairs near the Dirac point [ $\mathbf{k}$  states satisfying  $\Theta(\mathbf{k}) \approx 0$  on the cutting line; see Fig. 4(a)] are hardly excited. Instead, high-energy electron-hole pairs [ $\mathbf{k}$  states of  $\Theta(\mathbf{k}) \approx \pm \pi/2$ ] do contribute to the frequency softening. Putting Eq. (18) into Eq. (2), we calculate the frequency shift as a function of  $E_F$  for a (9,0) zigzag SWNT. In Fig. 4(b), we plot  $\omega^{(0)}$  (black line) and  $\omega$  for room temperature (red curve) and  $\omega$  for 10 K (blue curve). The frequency difference between  $E_F=0.6$  eV and the Dirac point ( $E_F=0$ ) is about  $10 \text{ cm}^{-1}$ .

It is useful to compare Eq. (18) with the amplitude of electron-hole pair creation by the  $\Gamma$  point LO/TO phonon

modes in order to understand the diameter dependence of the RBM frequency shift of a zigzag SWNT. In a previous paper,<sup>26</sup> we obtained for zigzag SWNTs that

$$\langle eh(\mathbf{k})|\mathcal{H}_{\text{ep}}|\omega_{\text{LO}}\rangle = -ig_{\text{off}}\frac{u_{\text{LO}}}{a_{\text{cc}}}\sin\Theta(\mathbf{k}),$$

$$\langle eh(\mathbf{k})|\mathcal{H}_{\text{ep}}|\omega_{\text{TO}}\rangle = -ig_{\text{off}}\frac{u_{\text{TO}}}{a_{\text{cc}}}\cos\Theta(\mathbf{k}), \quad (19)$$

where  $u_{\text{LO}}$  ( $u_{\text{TO}}$ ) is the amplitude of the LO(TO)-phonon mode. The  $\Theta(\mathbf{k})$  dependence of the matrix element of Eq. (18) is the same as the  $\Gamma$  point LO mode of Eq. (19). By comparing Eq. (18) with Eq. (19), we find that the ratio of the el-ph matrix element squared is given by

$$R = \frac{|\langle eh(\mathbf{k})|\mathcal{H}_{\text{ep}}|\omega^{(0)}\rangle|^2}{|\langle eh(\mathbf{k})|\mathcal{H}_{\text{ep}}|\omega_{\text{LO}}\rangle|^2} = \left(\frac{s_z a_{\text{cc}}}{d_t u_{\text{LO}}}\right)^2. \quad (20)$$

Since the phonon amplitude is proportional to the phonon frequency as  $s_z \propto \sqrt{\hbar/M\omega^{(0)}}$  and  $u_{\text{LO}} \propto \sqrt{\hbar/M\omega_{\text{LO}}}$  ( $M$  is the mass of the carbon atom), we obtain from Eq. (20) that

$$R \approx \frac{a_{\text{cc}}}{d_t}. \quad (21)$$

Here, we have used Eq. (1) and  $\omega_{\text{LO}}=1600 \text{ cm}^{-1}$  to get  $s_z^2/u_{\text{LO}}^2 = \omega_{\text{LO}}/\omega^{(0)} \approx 7.2(d_t/1 \text{ nm})$ . Because the squared matrix element appears in the numerator of Eq. (2), the RBM frequency shift is proportional to the inverse of  $d_t$ . This is consistent with the fact that the RBM frequency shift of a (9,0) SWNT is around  $10 \text{ cm}^{-1}$  because the frequency shift of the  $\Gamma$  point LO mode<sup>26</sup> reaches around  $50 \text{ cm}^{-1}$  and  $R \approx 0.2$ . The frequency difference between  $E_F=0.6 \text{ eV}$  and the Dirac point is about  $5 \text{ cm}^{-1}$  for a (18,0) zigzag SWNT ( $d_t \approx 1.4 \text{ nm}$ ), whose  $d_t$  is twice the  $d_t$  of a (9,0) SWNT. It is expected that the frequency shift of the RBM in zigzag SWNTs is expressed by  $50(a_{\text{cc}}/d_t) \text{ cm}^{-1}$ .

In Fig. 4(b), the decay width is zero because there is no electron-hole pair satisfying  $E < \hbar\omega^{(0)}$  [see Figs. 4(a) and 2(b)]. In principle, the decay width due to the el-ph interaction is absent for zigzag SWNTs when  $d_t \lesssim 2 \text{ nm}$  because the curvature-induced energy gap is larger than the original RBM phonon energy:  $E_{\text{gap}} \gg \hbar\omega^{(0)}$ . On the other hand, when  $d_t > 2 \text{ nm}$ , we have checked that the  $\Gamma$  value is less than  $1 \text{ cm}^{-1}$  due to the small matrix element for a larger diameter zigzag SWNT.

For a general  $(n,m)$  SWNT with a chiral angle  $\theta$ , the el-ph interaction for the RBM becomes

$$\mathcal{H}_{\text{ep}}(\theta) = \frac{2s_z}{d_t} \begin{pmatrix} g_{\text{on}} & -\frac{g_{\text{off}}}{2}e^{+i3\theta} \\ -\frac{g_{\text{off}}}{2}e^{-i3\theta} & g_{\text{on}} \end{pmatrix}, \quad (22)$$

which is derived in Appendix B. As a result, the matrix element for an electron-hole pair creation is chirality dependent as

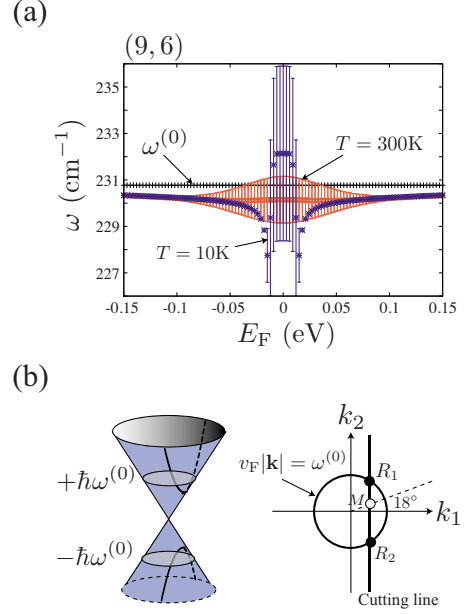


FIG. 5. (Color online) (a) The  $E_F$  dependence of the RBM frequency in the case of the (9,6) chiral SWNT at room temperature (red curve) and at 10 K (blue curve). We plot  $\omega^{(0)}$  as the black line for comparison. (b) The decay width ( $\Gamma$ ) is nonzero because of  $E_{\text{gap}} < \hbar\omega^{(0)}$ . At the  $R_1$  and  $R_2$  points, there is the contribution to  $\Gamma$ . At  $M$  [ $\Theta(\mathbf{k})=18^\circ$ ] the contribution to phonon softening becomes a maximum.

$$\langle eh(\mathbf{k})|\mathcal{H}_{\text{ep}}(\theta)|\omega^{(0)}\rangle = ig_{\text{off}}\frac{s_z}{d_t}\sin[\Theta(\mathbf{k}) + 3\theta], \quad (23)$$

where  $k_1=|\mathbf{k}|\cos\Theta(\mathbf{k})$  is the wave vector in the direction around the tube axis and  $k_2=|\mathbf{k}|\sin\Theta(\mathbf{k})$  is the one along the tube axis. Thus the frequency shift of the RBM has a chiral angle dependence. In particular, armchair SWNTs ( $\theta=30^\circ$ ) exhibit neither any frequency shift nor broadening, regardless of their diameters because the el-ph matrix element becomes

$$\langle eh(\mathbf{k})|\mathcal{H}_{\text{ep}}(\theta)|\omega^{(0)}\rangle = ig_{\text{off}}\frac{s_z}{d_t}\cos[\Theta(\mathbf{k})], \quad (24)$$

which is zero for a cutting line of the metallic band:  $\Theta(\mathbf{k}) = \pm\pi/2$ . This  $\Theta(\mathbf{k})$  dependence of Eq. (24) is the same as that of the TO-phonon mode of Eq. (19) and the absence of the frequency shift of the RBM in armchair SWNTs is similar to that of the  $\Gamma$  point TO mode in armchair SWNTs.<sup>26</sup>

In Fig. 5(a) we show the frequency shift in a (9,6) SWNT ( $\theta=24^\circ$ ). The factor of  $\sin[\Theta(\mathbf{k})+3\theta]$  in Eq. (23) indicates that low-energy electron-hole pairs satisfying  $\Theta(\mathbf{k}) \approx \pi/2 - 3\theta=18^\circ$  on the cutting line contribute significantly to the frequency shift. The decay width is nonzero because an electron-hole pair can be excited near  $E \approx \hbar\omega^{(0)}$  [see Figs. 5(b) and 2(b)].

Our numerical calculation shows that the RBM of a (14,2) chiral SWNT exhibits an  $E_F$ -dependent frequency shift of about  $3 \text{ cm}^{-1}$  within an  $E_F$  range of  $\pm 0.3 \text{ eV}$ . This result is consistent with the experimental result by Nguyen *et al.*,<sup>13</sup> who observed that the RBM of a (14,2) chiral tube exhibits a

small gate-dependent frequency up shift up to  $3 \text{ cm}^{-1}$  within the gate voltage range of  $\pm 1 \text{ eV}$ , if we assume that the change in the gate voltage of  $\pm 1 \text{ V}$  corresponds to  $E_F \approx \pm 0.3 \text{ eV}$ , namely, the gate efficiency factor is about 0.3.

### A. Raman intensity

We note that Eq. (21) does not mean that the Raman intensity of the RBM is much smaller than that of the LO/TO-phonon modes. The Raman intensity is relevant to the el-ph matrix element for a photoexcited electron within the conduction states,

$$\begin{aligned}
 & \langle ee(\mathbf{k}) | \mathcal{H}_{\text{ep}} | \omega^{(0)} \rangle \\
 &= \int [\psi_{c,\mathbf{k}}^K(\mathbf{r})]^\dagger \mathcal{H}_{\text{ep}} \psi_{c,\mathbf{k}}^K(\mathbf{r}) d^2\mathbf{r} \\
 &= \frac{s_z}{2r} \begin{bmatrix} e^{+i[\Theta(\mathbf{k})/2]} \\ -e^{-i[\Theta(\mathbf{k})/2]} \end{bmatrix}_t \begin{pmatrix} g_{\text{on}} & -\frac{g_{\text{off}}}{2} e^{+i3\theta} \\ -\frac{g_{\text{off}}}{2} e^{-i3\theta} & g_{\text{on}} \end{pmatrix} \\
 & \quad \times \begin{bmatrix} e^{-i[\Theta(\mathbf{k})/2]} \\ -e^{+i[\Theta(\mathbf{k})/2]} \end{bmatrix} \\
 &= \frac{s_z}{d_t} \{2g_{\text{on}} + g_{\text{off}} \cos[\Theta(\mathbf{k}) + 3\theta]\}. \quad (25)
 \end{aligned}$$

In this case, the  $g_{\text{on}}$  term does contribute to the matrix element and enhances the Raman intensity. Although Eq. (25) is chirality dependent, the dependence is small since  $2g_{\text{on}} \gg g_{\text{off}}$ . We compare this result with the corresponding LO mode el-ph matrix element from a conduction state to a conduction state in zigzag or armchair SWNTs near the  $K$  point,<sup>26</sup>

$$\langle ee(\mathbf{k}) | \mathcal{H}_{\text{ep}} | \omega_{\text{LO}} \rangle = i g_{\text{off}} \frac{u_{\text{LO}}}{a_{\text{cc}}} \cos \Theta(\mathbf{k}). \quad (26)$$

The ratio between Eqs. (25) and (26) becomes

$$\frac{|\langle ee(\mathbf{k}) | \mathcal{H}_{\text{ep}} | \omega^{(0)} \rangle|}{|\langle ee(\mathbf{k}) | \mathcal{H}_{\text{ep}} | \omega_{\text{LO}} \rangle|} \approx \frac{g_{\text{on}} a_{\text{cc}} s_z}{g_{\text{off}} r u_{\text{LO}}} \approx 5 \sqrt{\frac{a_{\text{cc}}}{d_t}}, \quad (27)$$

which means that the intensity of the RBM can be comparable to that of the  $G$  band because the intensity ratio is given by

$$\frac{I_{\text{RBM}}}{I_G} \equiv \frac{|\langle ee(\mathbf{k}) | \mathcal{H}_{\text{ep}} | \omega^{(0)} \rangle|^2}{|\langle ee(\mathbf{k}) | \mathcal{H}_{\text{ep}} | \omega_{\text{LO}} \rangle|^2} \approx \frac{3.5 \text{ (nm)}}{d_t}. \quad (28)$$

Here we assume that  $I_{\text{RBM}}$  and  $I_G$  are taken for each resonant conditions, respectively. When the laser energy is resonant only for the  $G$  band, for example, then  $I_{\text{RBM}}$  is negligible as compared with  $I_G$  as observed by Paillet *et al.*<sup>44</sup>

When  $\pi$  electrons satisfying  $\theta(\mathbf{k}_{ij}) \approx 0$  contribute to the intensity most effectively, the intensity of the RBM is maximum for zigzag nanotubes ( $\theta=0$ ) and is minimum for armchair nanotubes ( $\theta=\pi/6$ ). The same tendency was observed by the experiment of Strano *et al.*<sup>34</sup> and was confirmed by a first-principles calculation by Machon *et al.*<sup>45</sup> On the other

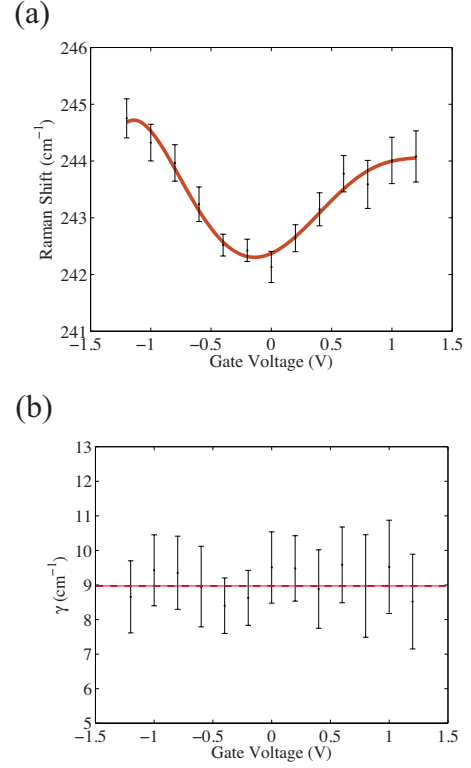


FIG. 6. (Color online) (a) The RBM frequency and (b) the spectral width as a function of the gate voltage for an isolated SWNT. The laser excitation energy is 2.15 eV. The  $(n,m)$  value of the SWNT is assigned as (11,2) or (12,0).

hand, the frequency shift of the RBM is absent for armchair nanotubes while that for zigzag nanotubes is a maximum.

## V. EXPERIMENT

We next compare our theoretical results with experimental Raman RBM data taken for an individual SWNT as a function of the gate voltage with the laser excitation energy of 2.15 eV. In Fig. 6(a), we show a plot of the RBM Raman frequency as a function of the gate voltage. It should be noted that the  $E_{ii}$  values seem to be modified slightly as a function of the gate voltage, which changes the Raman intensity. The experimental details relevant to Fig. 6 will be reported elsewhere.<sup>46</sup>

Here we note that the Raman frequency in Fig. 6(a) shows a minimum value at zero gate voltage, while the spectral width in Fig. 6(b) appears to be constant within the error bars. The gate voltage-independent offset of the spectra width does not originate from the RBM phonon self-energy due to the electron-hole pair creation but rather from the lifetime of a photoexcited carrier. The absence of a gate voltage-dependent broadening shows that  $E_{\text{gap}}$  is larger than  $\hbar\omega^{(0)}$ . This is consistent with the fact that the  $(n,m)$  for this SWNT is assigned as (11,2) or (12,0) using a Kataura plot based on the extended tight-binding model.<sup>36</sup> In fact, as shown in Fig. 2(b), the calculated  $E_{\text{gap}}$  [62 meV for (11,2), 68 meV for (12,0)] is larger than the RBM energy ( $\hbar\omega^{(0)} \approx 30 \text{ meV}$ ). The RBM frequency difference between the

gate voltage of 0 V and of 1 V is about  $2.5 \text{ cm}^{-1}$ , which is close to our theoretical estimation for a (11,2) or (12,0) SWNT if the gate coupling efficiency factor of this SWNT is about 0.2. We estimated the gate coupling efficiency to be about 0.2 for this sample using Eq. (29) in Ref. 22, which is an estimation based on the voltage window in which the  $G^-$  broadens.<sup>46</sup> In this case, a frequency shift is estimated to be about  $2.4 \text{ cm}^{-1}$  for a (12,0) SWNT from  $(E_F/0.6 \text{ eV})50(a_{cc}/d_t) \text{ cm}^{-1}$  with  $E_F=0.2 \text{ eV}$  and  $d_t \approx 0.93 \text{ nm}$ . The sample does not exhibit a perfect symmetric shape for the RBM frequency about positive and negative gate voltage values but shows some asymmetric shape. This asymmetry cannot be explained by the phonon self-energy. We think that the asymmetry is due to a change in a spring force constant by doping.

## VI. DISCUSSION AND SUMMARY

Let us discuss the similarity between the RBM and the LO/TO-phonon modes for achiral SWNTs. The RBM matrix element of Eq. (23) shows that the  $\Theta(\mathbf{k})$  dependence is the same as the LO (TO) matrix element of Eq. (19) when  $\theta = 0^\circ$  ( $\theta = 30^\circ$ ). As a result, we obtain using Eq. (21) that

$$\omega_{\text{RBM}}^{(2)} \approx \omega_{\text{LO}}^{(2)} \frac{a_{cc}}{d_t}, \quad (29)$$

for zigzag SWNTs. This correspondence originates from the character of the RBM as an optical-phonon mode like the LO/TO modes; that is, the  $A$  and  $B$  atoms oscillate in the opposite circumferential directions. For chiral SWNTs ( $\theta \neq 0^\circ$  or  $30^\circ$ ), on the other hand, the relationship between the RBM and the LO/TO is not as straightforward as that for achiral SWNTs because the LO/TO-phonon eigenvector is not pointing along either the nanotube axis or the circumference.<sup>47</sup> This changes the  $\Theta(\mathbf{k})$  dependence in the LO (TO) matrix element of Eq. (19) as

$$\begin{aligned} \langle \text{eh}(\mathbf{k}) | \mathcal{H}_{\text{ep}} | \omega_{\text{LO}} \rangle &= -ig_{\text{off}} \frac{u_{\text{LO}}}{a_{cc}} \sin[\Theta(\mathbf{k}) + \phi], \\ \langle \text{eh}(\mathbf{k}) | \mathcal{H}_{\text{ep}} | \omega_{\text{TO}} \rangle &= -ig_{\text{off}} \frac{u_{\text{TO}}}{a_{cc}} \cos[\Theta(\mathbf{k}) + \phi], \end{aligned} \quad (30)$$

where  $\phi$  is a parameter for the phonon eigenvector.<sup>26</sup> If we consider the frequency shift for  $|E_F| \geq \hbar \omega_{\text{LO(TO)}/2}$ , only high-energy electron-hole pairs contribute to the frequency shift. Then, by rewriting Eq. (23) using Eq. (30), and putting the result into Eq. (2), we obtain using Eq. (21) that

$$\omega_{\text{RBM}}^{(2)} \approx \omega_{\text{LO}}^{(2)} \frac{a_{cc}}{d_t} \cos^2(3\theta - \phi), \quad (31)$$

where we assume  $\phi \leq 30^\circ$  which results in  $|\omega_{\text{TO}}^{(2)}| \ll |\omega_{\text{LO}}^{(2)}|$ . We note that the relationship between the frequency shift of the RBM and that of an optical-phonon mode, which is similar to Eq. (31), was also derived by Nisoli *et al.*<sup>48</sup>

We have shown that the electron-hole pair creation is given by the off-site deformation potential, whose effect is represented by the deformation-induced gauge field  $\mathbf{A}(\mathbf{r})$ . It

is naturally expected that electron-hole pair creation is enhanced where the deformation-induced gauge field appears. A static  $\mathbf{A}(\mathbf{r})$  field appears near the boundary (edge) of the sample.<sup>41</sup> We will study the effect of the edge on the phonon frequency shift in the future.

Finally we discuss the effect of impurities on the RBM frequency. When impurities are approximated by adding  $V(\mathbf{r})\sigma_0$  to the effective-mass Hamiltonian of Eq. (4), then it can be shown that the broadening of the RBM due to the el-ph interaction is not enhanced by the presence of impurities. It is because of this that the wave function of a conduction state relates to the wave function of a valence state by multiplying  $\sigma_z$  (particle-hole symmetry), and therefore the matrix element of  $V(\mathbf{r})\sigma_0$  between a conduction state and a valence state vanishes. In contrast, the Coulomb interaction between an electron and a hole may contribute to the broadening of the RBM since an electron and a hole in the intermediate state are attracted to each other, which affects the lifetime of the RBM.

In summary, for a fixed diameter metallic tube, a zigzag SWNT exhibits the maximum RBM frequency shift and an armchair SWNT does not show any frequency shift. This is due to the chirality-dependent el-ph interaction for the RBM. For a zigzag SWNT, the frequency softening is about  $10 \text{ cm}^{-1}$  in a (9,0) SWNT and it is proportional to the inverse of the diameter. When  $d_t \lesssim 2 \text{ nm}$ , no broadening of the RBM spectra appears, since the curvature-induced energy gap is larger than the RBM phonon energy. (9,6) and (10,7) SWNTs are candidates which can exhibit a broadening since the curvature-induced energy gap is smaller than the RBM energy. Although the frequency shift of the RBM is much smaller than that of the  $\Gamma$  point optical-phonon mode, the frequency shift of the RBM as a function of the Fermi energy shows a characteristic behavior depending on the relative position of the cutting line with respect to the Dirac point.

## ACKNOWLEDGMENTS

R.S. acknowledges a Grant-in-Aid (Grants No. 16076201 and No. 20241023) from MEXT. MIT authors acknowledge support from NSF under Grant No. DMR 07-04197.

## APPENDIX A: EFFECTIVE-MASS THEORY WITH LATTICE DEFORMATION

In this appendix we derive Eqs. (8) and (9) from the nearest-neighbor tight-binding Hamiltonian of a graphene sheet with a lattice deformation. When a graphene sheet does not have any lattice deformation, the Hamiltonian of  $\pi$  electrons is modeled by

$$\mathcal{H}_0 = -\gamma_0 \sum_{i \in A} \sum_{a=1,2,3} [(c_{i+a}^B)^\dagger c_i^A + (c_i^A)^\dagger c_{i+a}^B]. \quad (\text{A1})$$

We use the Bloch theorem to diagonalize Eq. (A1). The Bloch wave function with wave vector  $\mathbf{k}$  is defined by

$$|\Psi_s^{\mathbf{k}}\rangle = \frac{1}{\sqrt{N_u}} \sum_{i \in s} e^{i\mathbf{k}\cdot\mathbf{r}_i} (c_i^\dagger)^\dagger |0\rangle \quad (s=A,B), \quad (\text{A2})$$

where  $N_u$  is the number of hexagonal unit cells and  $|0\rangle$  denotes the state of carbon atoms without  $\pi$  electrons. The off-site matrix element of  $\mathcal{H}_0$  is given by

$$\begin{aligned} \langle \Psi_A^{\mathbf{k}} | \mathcal{H}_0 | \Psi_B^{\mathbf{k}} \rangle &= -\gamma_0 \sum_{a=1,2,3} f_a(\mathbf{k}) = -\gamma_0 f(\mathbf{k}), \\ \langle \Psi_B^{\mathbf{k}} | \mathcal{H}_0 | \Psi_A^{\mathbf{k}} \rangle &= -\gamma_0 \sum_{a=1,2,3} f_a(\mathbf{k})^* = -\gamma_0 f(\mathbf{k})^*, \end{aligned} \quad (\text{A3})$$

where  $f_a(\mathbf{k}) \equiv e^{i\mathbf{k}\cdot\mathbf{R}_a}$  and  $f(\mathbf{k}) \equiv \sum_{a=1,2,3} f_a(\mathbf{k})$ ,<sup>10</sup> and the on-site matrix element of  $\mathcal{H}_0$ ,  $\langle \Psi_s^{\mathbf{k}} | \mathcal{H}_0 | \Psi_s^{\mathbf{k}} \rangle$  ( $s=A,B$ ), can be taken as zero. The energy eigenvalue is written in  $2 \times 2$  matrix form as

$$E(\mathbf{k}) \begin{pmatrix} |\Psi_A^{\mathbf{k}}\rangle \\ |\Psi_B^{\mathbf{k}}\rangle \end{pmatrix} = -\gamma_0 \begin{pmatrix} 0 & f(\mathbf{k}) \\ f(\mathbf{k})^* & 0 \end{pmatrix} \begin{pmatrix} |\Psi_A^{\mathbf{k}}\rangle \\ |\Psi_B^{\mathbf{k}}\rangle \end{pmatrix}. \quad (\text{A4})$$

The energy-band structure of  $\mathcal{H}_0$  is obtained by solving

$$\det \begin{pmatrix} E(\mathbf{k}) & \gamma_0 f(\mathbf{k}) \\ \gamma_0 f(\mathbf{k})^* & E(\mathbf{k}) \end{pmatrix} = 0. \quad (\text{A5})$$

The solution  $E(\mathbf{k}) = +\gamma_0 |f(\mathbf{k})|$  ( $-\gamma_0 |f(\mathbf{k})|$ ) is the conduction (valence) energy band. The conduction energy band and the valence energy band touch each other where  $|f(\mathbf{k})|$  vanishes.  $|f(\mathbf{k})|=0$  is satisfied at the  $K$  point,  $\mathbf{k}_F = [(4\pi/3)\sqrt{3}a_{cc}, 0]$ , and at the  $K'$  point,  $-\mathbf{k}_F$ . The  $K$  or  $K'$  point is referred to as the Dirac point.

By expanding  $f_a(\mathbf{k})$  in Eq. (A3) around the wave vector of  $\mathbf{k}_F$  (the  $K$  point), we obtain  $f_a(\mathbf{k}_F + \mathbf{k}) = f_a(\mathbf{k}_F) + i f_a(\mathbf{k}_F) \mathbf{k} \cdot \mathbf{R}_a + \dots$ . Using  $\mathbf{k}_F = (4\pi/3)\sqrt{3}a_{cc}, 0$ , we get  $f_1(\mathbf{k}_F) = 1$ ,  $f_2(\mathbf{k}_F) = e^{-i2\pi/3}$ , and  $f_3(\mathbf{k}_F) = e^{+i2\pi/3}$ . Substituting these into Eq. (A3), we obtain

$$\begin{aligned} \langle \Psi_A^{\mathbf{k}_F + \mathbf{k}} | \mathcal{H}_0 | \Psi_B^{\mathbf{k}_F + \mathbf{k}} \rangle &= \gamma_0 \frac{3a_{cc}}{2} (k_x - ik_y) + \dots, \\ \langle \Psi_B^{\mathbf{k}_F + \mathbf{k}} | \mathcal{H}_0 | \Psi_A^{\mathbf{k}_F + \mathbf{k}} \rangle &= \gamma_0 \frac{3a_{cc}}{2} (k_x + ik_y) + \dots, \end{aligned} \quad (\text{A6})$$

where we used  $\langle \Psi_A^{\mathbf{k}_F} | \mathcal{H}_0 | \Psi_B^{\mathbf{k}_F} \rangle = -\gamma_0 f(\mathbf{k}_F) = 0$ . We neglect the correction indicated by  $\dots$  in Eq. (A6) which is of the order of  $\mathcal{O}(k^2)$  because we only consider  $\mathbf{k}$  states near the  $K$  point, namely,  $|\mathbf{k}| \ll |\mathbf{k}_F|$ .

From Eq. (A6), we see that Eq. (A4) is approximated by

$$\begin{aligned} E(\mathbf{k}_F + \mathbf{k}) \begin{pmatrix} |\Psi_A^{\mathbf{k}_F + \mathbf{k}}\rangle \\ |\Psi_B^{\mathbf{k}_F + \mathbf{k}}\rangle \end{pmatrix} \\ = \frac{3\gamma_0 a_{cc}}{2} \begin{pmatrix} 0 & k_x - ik_y \\ k_x + ik_y & 0 \end{pmatrix} \begin{pmatrix} |\Psi_A^{\mathbf{k}_F + \mathbf{k}}\rangle \\ |\Psi_B^{\mathbf{k}_F + \mathbf{k}}\rangle \end{pmatrix}. \end{aligned} \quad (\text{A7})$$

By introducing the Fermi velocity as  $v_F = 3\gamma_0 a_{cc}/2\hbar$ , the momentum operator  $\hat{\mathbf{p}} = -i\hbar\nabla$  and the Pauli matrix  $\boldsymbol{\sigma} = (\sigma_x, \sigma_y)$ , we obtain the effective-mass Hamiltonian as  $v_F \boldsymbol{\sigma} \cdot \hat{\mathbf{p}}$  which is given by Eq. (4).

A lattice deformation induces a local modification of the nearest-neighbor hopping integral as  $-\gamma_0 \rightarrow -\gamma_0 + \delta\gamma_0^a(\mathbf{r}_i)$  ( $a=1,2,3$ ) [see Fig. 3(a)]. We define this perturbation as Eq. (7). The off-site matrix element of  $\mathcal{H}_1$  with respect to the Bloch wave function of Eq. (A2) is given by

$$\begin{aligned} \langle \Psi_A^{\mathbf{k} + \delta\mathbf{k}} | \mathcal{H}_1 | \Psi_B^{\mathbf{k}} \rangle &= \frac{1}{N_u} \sum_{i \in A} \sum_{a=1,2,3} \delta\gamma_0^a(\mathbf{r}_i) f_a(\mathbf{k}) e^{-i\delta\mathbf{k}\cdot\mathbf{r}_i}, \\ \langle \Psi_B^{\mathbf{k} + \delta\mathbf{k}} | \mathcal{H}_1 | \Psi_A^{\mathbf{k}} \rangle &= \frac{1}{N_u} \sum_{i \in A} \sum_{a=1,2,3} \delta\gamma_0^a(\mathbf{r}_i) f_a(\mathbf{k})^* e^{-i\delta\mathbf{k}\cdot(\mathbf{r}_i + \mathbf{R}_a)}. \end{aligned} \quad (\text{A8})$$

By changing  $\mathbf{k}$  in Eq. (A8) to  $\mathbf{k}_F + \mathbf{k}$  and using  $f_a(\mathbf{k}_F + \mathbf{k}) = f_a(\mathbf{k}_F) + i f_a(\mathbf{k}_F) \mathbf{k} \cdot \mathbf{R}_a + \dots$ , we see that

$$\begin{aligned} \langle \Psi_A^{\mathbf{k}_F + \mathbf{k} + \delta\mathbf{k}} | \mathcal{H}_1 | \Psi_B^{\mathbf{k}_F + \mathbf{k}} \rangle \\ = \frac{1}{N_u} \sum_{i \in A} \sum_{a=1,2,3} \delta\gamma_0^a(\mathbf{r}_i) f_a(\mathbf{k}_F) e^{-i\delta\mathbf{k}\cdot\mathbf{r}_i} + \dots, \\ \langle \Psi_B^{\mathbf{k}_F + \mathbf{k} + \delta\mathbf{k}} | \mathcal{H}_1 | \Psi_A^{\mathbf{k}_F + \mathbf{k}} \rangle \\ = \frac{1}{N_u} \sum_{i \in A} \sum_{a=1,2,3} \delta\gamma_0^a(\mathbf{r}_i) f_a(\mathbf{k}_F)^* e^{-i\delta\mathbf{k}\cdot\mathbf{r}_i} + \dots. \end{aligned} \quad (\text{A9})$$

The correction indicated by  $\dots$  in Eq. (A9) is negligible when  $|\mathbf{k}| \ll |\mathbf{k}_F|$  and  $|\delta\mathbf{k}| \ll |\mathbf{k}_F|$ . Substituting  $f_1(\mathbf{k}_F) = 1$ ,  $f_2(\mathbf{k}_F) = e^{-i2\pi/3}$ , and  $f_3(\mathbf{k}_F) = e^{+i2\pi/3}$  into Eq. (A9), we get

$$\begin{aligned} \langle \Psi_A^{\mathbf{k}_F + \mathbf{k} + \delta\mathbf{k}} | \mathcal{H}_1 | \Psi_B^{\mathbf{k}_F + \mathbf{k}} \rangle &= \frac{v_F}{N_u} \sum_{i \in A} \{A_x(\mathbf{r}_i) - iA_y(\mathbf{r}_i)\} e^{-i\delta\mathbf{k}\cdot\mathbf{r}_i}, \\ \langle \Psi_B^{\mathbf{k}_F + \mathbf{k} + \delta\mathbf{k}} | \mathcal{H}_1 | \Psi_A^{\mathbf{k}_F + \mathbf{k}} \rangle &= \frac{v_F}{N_u} \sum_{i \in A} \{A_x(\mathbf{r}_i) + iA_y(\mathbf{r}_i)\} e^{-i\delta\mathbf{k}\cdot\mathbf{r}_i}, \end{aligned} \quad (\text{A10})$$

where  $\mathbf{A}(\mathbf{r}) = [A_x(\mathbf{r}), A_y(\mathbf{r})]$  is defined from  $\delta\gamma_0^a(\mathbf{r})$  ( $a=1,2,3$ ) as

$$\begin{aligned} v_F A_x(\mathbf{r}) &= \delta\gamma_0^1(\mathbf{r}) - \frac{1}{2} [\delta\gamma_0^2(\mathbf{r}) + \delta\gamma_0^3(\mathbf{r})], \\ v_F A_y(\mathbf{r}) &= \frac{\sqrt{3}}{2} [\delta\gamma_0^2(\mathbf{r}) - \delta\gamma_0^3(\mathbf{r})]. \end{aligned} \quad (\text{A11})$$

Equation (A10) shows that  $\mathcal{H}_1$  appears as  $v_F \boldsymbol{\sigma} \cdot \mathbf{A}(\mathbf{r})$  in the effective-mass Hamiltonian. Thus, the total Hamiltonian becomes  $v_F \boldsymbol{\sigma} \cdot [\hat{\mathbf{p}} + \mathbf{A}(\mathbf{r})]$ , which is given by Eq. (8).

## APPENDIX B: CHIRALITY DEPENDENCE OF THE ELECTRON-PHONON INTERACTION

Next we derive the el-ph interaction for the RBM in an  $(n,m)$  SWNT. A straightforward method to derive the effective-mass Hamiltonian for an  $(n,m)$  nanotube is to represent a vector in terms of unit vectors  $\mathbf{e}_1 = \mathbf{C}_h/|\mathbf{C}_h|$  and  $\mathbf{e}_2 = \mathbf{T}/|\mathbf{T}|$  instead of  $\mathbf{e}_x$  and  $\mathbf{e}_y$  [see Fig. 7(a)]. Here  $\mathbf{C}_h$  and  $\mathbf{T}$  are the chiral and translational vectors, respectively.<sup>10</sup> The relationship between  $(\mathbf{e}_1, \mathbf{e}_2)$  and  $(\mathbf{e}_x, \mathbf{e}_y)$  is given by the chiral angle as

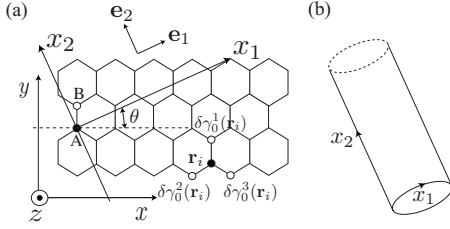


FIG. 7. (a) We define the coordinate system  $(x_1, x_2)$  for graphene.  $\mathbf{e}_1$  ( $\mathbf{e}_2$ ) is the dimensionless unit vector for the  $x_1$  axis ( $x_2$  axis). (b)  $x_1$  ( $x_2$ ) is the coordinate around (along) a tube axis. The periodic boundary condition along the  $x_1$  axis corresponds to a carbon nanotube with chiral angle  $\theta$ .

$$\begin{pmatrix} \mathbf{e}_x \\ \mathbf{e}_y \end{pmatrix} = \begin{pmatrix} \cos \theta & -\sin \theta \\ \sin \theta & \cos \theta \end{pmatrix} \begin{pmatrix} \mathbf{e}_1 \\ \mathbf{e}_2 \end{pmatrix}. \quad (\text{B1})$$

Using Eq. (B1), we represent  $\mathbf{R}_a$  ( $a=1,2,3$ ) in terms of  $\mathbf{e}_1$ ,  $\mathbf{e}_2$ , and  $\theta$  as

$$\begin{aligned} \frac{\mathbf{R}_1}{a_{cc}} &= \sin \theta \mathbf{e}_1 + \cos \theta \mathbf{e}_2, \\ \frac{\mathbf{R}_2}{a_{cc}} &= \left( -\frac{\sqrt{3}}{2} \cos \theta - \frac{1}{2} \sin \theta \right) \mathbf{e}_1 + \left( \frac{\sqrt{3}}{2} \sin \theta - \frac{1}{2} \cos \theta \right) \mathbf{e}_2, \\ \frac{\mathbf{R}_3}{a_{cc}} &= \left( \frac{\sqrt{3}}{2} \cos \theta - \frac{1}{2} \sin \theta \right) \mathbf{e}_1 + \left( -\frac{\sqrt{3}}{2} \sin \theta - \frac{1}{2} \cos \theta \right) \mathbf{e}_2. \end{aligned} \quad (\text{B2})$$

Then, by following the same procedure to get Eq. (A6) of Appendix A, we obtain

$$\begin{aligned} \langle \Psi_A^{\mathbf{k}_F+\mathbf{k}} | \mathcal{H}_0 | \Psi_B^{\mathbf{k}_F+\mathbf{k}} \rangle &= e^{-i\theta} \gamma_0 \frac{3a_{cc}}{2} (k_1 - ik_2) + \dots, \\ \langle \Psi_B^{\mathbf{k}_F+\mathbf{k}} | \mathcal{H}_0 | \Psi_A^{\mathbf{k}_F+\mathbf{k}} \rangle &= e^{+i\theta} \gamma_0 \frac{3a_{cc}}{2} (k_1 + ik_2) + \dots, \end{aligned} \quad (\text{B3})$$

where we denote the wave vector in the direction around (along) the tube axis  $k_1$  ( $k_2$ ) that is  $\mathbf{k} = k_1 \mathbf{e}_1 + k_2 \mathbf{e}_2$  [see Figs. 7(a) and 7(b)].

Let us introduce another Bloch wave function which is defined by adding a chiral angle-dependent phase to the original Bloch wave function of Eq. (A2) as

$$\begin{aligned} |\Psi_A^{\mathbf{k}}(\theta)\rangle &= e^{-i\theta/2} |\Psi_A^{\mathbf{k}}\rangle, \\ |\Psi_B^{\mathbf{k}}(\theta)\rangle &= e^{+i\theta/2} |\Psi_B^{\mathbf{k}}\rangle. \end{aligned} \quad (\text{B4})$$

Then the effective-mass Hamiltonian becomes

$$v_F (\sigma_x p_1 + \sigma_y p_2), \quad (\text{B5})$$

and Eq. (A10) becomes

$$\begin{aligned} \langle \Psi_A^{\mathbf{k}_F+\mathbf{k}+\delta\mathbf{k}}(\theta) | \mathcal{H}_1 | \Psi_B^{\mathbf{k}_F+\mathbf{k}}(\theta) \rangle \\ = \frac{v_F}{N_{ui \in A}} \sum e^{+i\theta} \{A_x(\mathbf{r}_i) - iA_y(\mathbf{r}_i)\} e^{-i\delta\mathbf{k} \cdot \mathbf{r}_i}, \end{aligned}$$

$$\begin{aligned} \langle \Psi_B^{\mathbf{k}_F+\mathbf{k}+\delta\mathbf{k}}(\theta) | \mathcal{H}_1 | \Psi_A^{\mathbf{k}_F+\mathbf{k}}(\theta) \rangle \\ = \frac{v_F}{N_{ui \in A}} \sum e^{-i\theta} \{A_x(\mathbf{r}_i) + iA_y(\mathbf{r}_i)\} e^{-i\delta\mathbf{k} \cdot \mathbf{r}_i}. \end{aligned} \quad (\text{B6})$$

Therefore, by introducing  $A_1(\mathbf{r})$  and  $A_2(\mathbf{r})$  which are defined by

$$\begin{pmatrix} A_1(\mathbf{r}) \\ A_2(\mathbf{r}) \end{pmatrix} = \begin{pmatrix} \cos \theta & \sin \theta \\ -\sin \theta & \cos \theta \end{pmatrix} \begin{pmatrix} A_x(\mathbf{r}) \\ A_y(\mathbf{r}) \end{pmatrix}, \quad (\text{B7})$$

we see that the off-site interaction can be written as

$$\mathcal{H}_1^K = \sigma_x A_1(\mathbf{r}) + \sigma_y A_2(\mathbf{r}). \quad (\text{B8})$$

The Hamiltonian for a chiral SWNT can be represented by

$$v_F \boldsymbol{\sigma} \cdot [\mathbf{p} + \mathbf{A}(\mathbf{r})], \quad (\text{B9})$$

where  $\mathbf{p} = (p_1, p_2)$  and  $\mathbf{A}(\mathbf{r}) = [A_1(\mathbf{r}), A_2(\mathbf{r})]$ .

To determine  $A_1(\mathbf{r})$  and  $A_2(\mathbf{r})$ , it is necessary to represent  $A_x(\mathbf{r})$  and  $A_y(\mathbf{r})$  in the different coordinate system. We shall do this for obtaining the el-ph interaction for the RBM. Putting Eq. (B2) into

$$\delta\gamma_0^{\mu}(\mathbf{r}) \approx \frac{g_{\text{off}}}{\ell a_{cc}} \mathbf{R}_a \cdot [(\mathbf{R}_a \cdot \nabla) \mathbf{s}(\mathbf{r})], \quad (\text{B10})$$

of Eq. (11), we get using Eq. (9)

$$\begin{aligned} v_F A_x(\mathbf{r}) &= \frac{g_{\text{off}}}{2} \left\{ \cos 2\theta \left( -\frac{\partial s_1(\mathbf{r})}{\partial x_1} + \frac{\partial s_2(\mathbf{r})}{\partial x_2} \right) \right. \\ &\quad \left. + \sin 2\theta \left( \frac{\partial s_1(\mathbf{r})}{\partial x_2} + \frac{\partial s_2(\mathbf{r})}{\partial x_1} \right) \right\}, \\ v_F A_y(\mathbf{r}) &= \frac{g_{\text{off}}}{2} \left\{ -\sin 2\theta \left( -\frac{\partial s_1(\mathbf{r})}{\partial x_1} + \frac{\partial s_2(\mathbf{r})}{\partial x_2} \right) \right. \\ &\quad \left. + \cos 2\theta \left( \frac{\partial s_1(\mathbf{r})}{\partial x_2} + \frac{\partial s_2(\mathbf{r})}{\partial x_1} \right) \right\}. \end{aligned} \quad (\text{B11})$$

Inserting Eq. (B11) into Eq. (B7), we see that

$$v_F \begin{pmatrix} A_1(\mathbf{r}) \\ A_2(\mathbf{r}) \end{pmatrix} = \frac{g_{\text{off}}}{2} \begin{pmatrix} \cos 3\theta & \sin 3\theta \\ -\sin 3\theta & \cos 3\theta \end{pmatrix} \begin{pmatrix} -\frac{\partial s_1(\mathbf{r})}{\partial x_1} + \frac{\partial s_2(\mathbf{r})}{\partial x_2} \\ \frac{\partial s_1(\mathbf{r})}{\partial x_2} + \frac{\partial s_2(\mathbf{r})}{\partial x_1} \end{pmatrix}. \quad (\text{B12})$$

The off-site el-ph interaction for the RBM of a chiral SWNT is given by replacing

$$\frac{\partial s_1(\mathbf{r})}{\partial x_1} \rightarrow \frac{\partial s_1(\mathbf{r})}{\partial x_1} + \frac{s_z}{r} \quad (\text{B13})$$

in Eq. (B12) as we have explained in Sec. III. For the  $\Gamma$  point RBM, since  $\partial s_1(\mathbf{r})/\partial x_i = 0$  and  $\partial s_2(\mathbf{r})/\partial x_i = 0$  ( $i=1,2$ ), we obtain  $v_F A_1 = -g_{\text{off}}(s_z/d_i) \cos 3\theta$  and  $v_F A_2 = g_{\text{off}}(s_z/d_i) \sin 3\theta$ . This gives the el-ph interaction written in Eq. (22).

- <sup>1</sup>A. M. Rao *et al.*, *Science* **275**, 187 (1997).
- <sup>2</sup>M. A. Pimenta, A. Marucci, S. A. Empedocles, M. G. Bawendi, E. B. Hanlon, A. M. Rao, P. C. Eklund, R. E. Smalley, G. Dresselhaus, and M. S. Dresselhaus, *Phys. Rev. B* **58**, R16016 (1998).
- <sup>3</sup>Z. Yu and L. Brus, *J. Phys. Chem. B* **105**, 1123 (2001).
- <sup>4</sup>A. Jorio, R. Saito, J. H. Hafner, C. M. Lieber, M. Hunter, T. McClure, G. Dresselhaus, and M. S. Dresselhaus, *Phys. Rev. Lett.* **86**, 1118 (2001).
- <sup>5</sup>S. Doorn, D. Heller, P. Barone, M. Usrey, and M. Strano, *Appl. Phys. A: Mater. Sci. Process.* **78**, 1147 (2004).
- <sup>6</sup>M. S. Dresselhaus, G. Dresselhaus, R. Saito, and A. Jorio, *Phys. Rep.* **409**, 47 (2005).
- <sup>7</sup>A. C. Ferrari *et al.*, *Phys. Rev. Lett.* **97**, 187401 (2006).
- <sup>8</sup>J. Yan, Y. Zhang, P. Kim, and A. Pinczuk, *Phys. Rev. Lett.* **98**, 166802 (2007).
- <sup>9</sup>M. A. Pimenta, G. Dresselhaus, M. S. Dresselhaus, L. G. Cancado, A. Jorio, and R. Saito, *Phys. Chem. Chem. Phys.* **9**, 1276 (2007).
- <sup>10</sup>R. Saito, G. Dresselhaus, and M. Dresselhaus, *Physical Properties of Carbon Nanotubes* (Imperial College, London, 1998).
- <sup>11</sup>A. Jorio *et al.*, *Phys. Rev. B* **65**, 155412 (2002).
- <sup>12</sup>H. Farhat, H. Son, G. G. Samsonidze, S. Reich, M. S. Dresselhaus, and J. Kong, *Phys. Rev. Lett.* **99**, 145506 (2007).
- <sup>13</sup>K. T. Nguyen, A. Gaur, and M. Shim, *Phys. Rev. Lett.* **98**, 145504 (2007).
- <sup>14</sup>Y. Wu, J. Maultzsch, E. Knoesel, B. Chandra, M. Huang, M. Y. Sfeir, L. E. Brus, J. Hone, and T. F. Heinz, *Phys. Rev. Lett.* **99**, 027402 (2007).
- <sup>15</sup>A. Das, A. K. Sood, A. Govindaraj, A. M. Saitta, M. Lazzeri, F. Mauri, and C. N. R. Rao, *Phys. Rev. Lett.* **99**, 136803 (2007).
- <sup>16</sup>O. Dubay, G. Kresse, and H. Kuzmany, *Phys. Rev. Lett.* **88**, 235506 (2002).
- <sup>17</sup>S. Piscanec, M. Lazzeri, F. Mauri, A. C. Ferrari, and J. Robertson, *Phys. Rev. Lett.* **93**, 185503 (2004).
- <sup>18</sup>M. Lazzeri and F. Mauri, *Phys. Rev. Lett.* **97**, 266407 (2006).
- <sup>19</sup>K. Ishikawa and T. Ando, *J. Phys. Soc. Jpn.* **75**, 084713 (2006).
- <sup>20</sup>V. N. Popov and P. Lambin, *Phys. Rev. B* **73**, 085407 (2006).
- <sup>21</sup>M. Lazzeri, S. Piscanec, F. Mauri, A. C. Ferrari, and J. Robertson, *Phys. Rev. B* **73**, 155426 (2006).
- <sup>22</sup>N. Caudal, A. M. Saitta, M. Lazzeri, and F. Mauri, *Phys. Rev. B* **75**, 115423 (2007).
- <sup>23</sup>M. Calandra and F. Mauri, *Phys. Rev. B* **76**, 205411 (2007).
- <sup>24</sup>S. Piscanec, M. Lazzeri, J. Robertson, A. C. Ferrari, and F. Mauri, *Phys. Rev. B* **75**, 035427 (2007).
- <sup>25</sup>T. Ando, *J. Phys. Soc. Jpn.* **77**, 014707 (2008).
- <sup>26</sup>K. I. Sasaki, R. Saito, G. Dresselhaus, M. S. Dresselhaus, H. Farhat, and J. Kong, *Phys. Rev. B* **77**, 245441 (2008).
- <sup>27</sup>C. Fantini, A. Jorio, M. Souza, M. S. Strano, M. S. Dresselhaus, and M. A. Pimenta, *Phys. Rev. Lett.* **93**, 147406 (2004).
- <sup>28</sup>H. Telg, J. Maultzsch, S. Reich, F. Hennrich, and C. Thomsen, *Phys. Rev. Lett.* **93**, 177401 (2004).
- <sup>29</sup>R. Saito, M. Fujita, G. Dresselhaus, and M. S. Dresselhaus, *Phys. Rev. B* **46**, 1804 (1992).
- <sup>30</sup>M. Ouyang, J.-L. Huang, C. L. Cheung, and C. M. Lieber, *Science* **292**, 702 (2001).
- <sup>31</sup>O. Gülseren, T. Yildirim, and S. Ciraci, *Phys. Rev. B* **65**, 153405 (2002).
- <sup>32</sup>H. Suzuura and T. Ando, *Phys. Rev. B* **65**, 235412 (2002).
- <sup>33</sup>J. Jiang, R. Saito, G. G. Samsonidze, S. G. Chou, A. Jorio, G. Dresselhaus, and M. S. Dresselhaus, *Phys. Rev. B* **72**, 235408 (2005).
- <sup>34</sup>M. Strano, S. Doorn, E. Haroz, C. Kittrell, R. Hauge, and R. Smalley, *Nano Lett.* **3**, 1091 (2003).
- <sup>35</sup>S. Bachilo, M. Strano, C. Kittrell, R. Hauge, R. Smalley, and R. Weisman, *Science* **298**, 2361 (2002).
- <sup>36</sup>G. G. Samsonidze, R. Saito, N. Kobayashi, A. Grüneis, J. Jiang, A. Jorio, S. G. Chou, G. Dresselhaus, and M. S. Dresselhaus, *Appl. Phys. Lett.* **85**, 5703 (2004).
- <sup>37</sup>C. L. Kane and E. J. Mele, *Phys. Rev. Lett.* **78**, 1932 (1997).
- <sup>38</sup>L. Yang, M. P. Anantram, J. Han, and J. P. Lu, *Phys. Rev. B* **60**, 13874 (1999).
- <sup>39</sup>L. Yang and J. Han, *Phys. Rev. Lett.* **85**, 154 (2000).
- <sup>40</sup>K. Sasaki, Y. Kawazoe, and R. Saito, *Prog. Theor. Phys.* **113**, 463 (2005).
- <sup>41</sup>K. Sasaki, S. Murakami, and R. Saito, *J. Phys. Soc. Jpn.* **75**, 074713 (2006).
- <sup>42</sup>D. Porezag, T. Frauenheim, T. Köhler, G. Seifert, and R. Kaschner, *Phys. Rev. B* **51**, 12947 (1995).
- <sup>43</sup>Ken-ichi Sasaki, Kentaro Sato, Riichiro Saito, Jie Jiang, Seiichiro Onari, and Yukio Tanaka, *Phys. Rev. B* **75**, 235430 (2007).
- <sup>44</sup>M. Paillet, T. Michel, J. C. Meyer, V. N. Popov, L. Henrard, S. Roth, and J.-L. Sauvajol, *Phys. Rev. Lett.* **96**, 257401 (2006).
- <sup>45</sup>M. Machón, S. Reich, H. Telg, J. Maultzsch, P. Ordejón, and C. Thomsen, *Phys. Rev. B* **71**, 035416 (2005).
- <sup>46</sup>H. Farhat, K. Sasaki, M. Kalbac, R. Saito, M. Dresselhaus, and J. Kong, (unpublished).
- <sup>47</sup>S. Reich, C. Thomsen, and P. Ordejón, *Phys. Rev. B* **64**, 195416 (2001).
- <sup>48</sup>C. Nisoli, P. E. Lammert, E. Mockensturm, and V. H. Crespi, *Phys. Rev. Lett.* **99**, 045501 (2007).